Hindawi
Journal of Applied Mathematics
Volume 2022, Article ID 8553330, 13 pages
https://doi.org/10.1155/2022/8553330

Research Article

Application of DTCWT Decomposition and Partial Differential Equation Denoising Methods in Remote Sensing Image Big Data Denoising and Reconstruction

Wei Zeng

College of Preparatory Education, Southwest Minzu University, Chengdu 610041, China

Correspondence should be addressed to Wei Zeng; 22700028@swun.edu.cn

Received 24 August 2022; Revised 10 October 2022; Accepted 18 October 2022; Published 27 October 2022

Academic Editor: Sheng Zhang

The precision of the traditional satellite remote sensing image denoising model cannot deal well with some precise production scenes. To solve this problem, this research proposes an improved remote sensing image processing model, in which the dual tree complex wavelet transform (DTCWT) method is used to conduct multiscale decomposition of the impact, and the fourth-order differential equation is used to denoise the decomposed complex high-frequency subband information, and then the denoised subbands are reconstructed into the denoised image. Through these two advanced signal-processing methods, the quality of reconstructed signals is improved and the noise content of various types is greatly reduced. The experimental results show that the normalized root mean square error of the denoising model designed in this study after training convergence is 0.02. When the noise variance is 0.030, the structure similarity, peak signal to noise ratio, and normalized signal to noise ratio are 0.74, 25.3, and 0.76, respectively, which are better than all other comparison models. The experimental data prove that the satellite remote sensing image data denoising model designed in this study has better denoising performance, and has certain application potential in high-precision satellite remote sensing image big data processing.

1. Introduction

With the formation of BeiDou satellite system and the expansion of commercial application, the era of big data in satellite industry based on satellite facility services is approaching. In this context, remote sensing images, as the basis of satellite big data industry, have attracted more and more attention to image quality. Therefore, the requirements of current civil scenes for remote sensing information extraction technology are also increasing [1]. However, remote sensing images will be interfered by various noises in remote sensing imaging, image transmission, and storage, resulting in the inability to accurately extract and use the features of ground objects in some images, which is not conducive to the commercial value mining of satellite remote sensing images [2, 3]. It can be seen that improving the denoising effect of remote sensing image data can increase the purity and readability of satellite remote sensing image data, thus making the subsequent application and processing easier, which has certain commercial value and research necessity. In 1983, Grant used multiscale functions to build the theoretical basis of multiwavelet methods, which greatly improved the degree of freedom of wavelet denoising methods [4]. In 1995, Sweldens improved the multiwavelet filtering algorithm. In this algorithm, the original signal is divided into odd and even parts, and filtered according to the classification of odd and even samples [5]. In 2000, Le Pennec and Mallat segmented the image according to Bandelet theory, making the wavelet filtering algorithm more effective [6]. In 2005, combined with the integer lattice theory, an image description method was designed to separate images at multiple scales and in multiple directions to achieve the optimal image block processing operation [7]. On the basis of previous research, this time, we creatively combined the DTCWT method with the fourth-order partial derivative equation to build a remote sensing image data denoising model. In the model, DTCWT is used to split the remote sensing image into complex low-frequency

subbands that contain almost no noise and complex high-frequency subbands that contain a lot of noise, and then partial differential is used to denoise the real part and imaginary part of the latter. Second-order difference method is used to solve the fourth-order partial differential iterative equation, so as to improve the denoising performance of the model on the premise of ensuring that the original image information is retained to the maximum extent. This is also the main academic contribution of this study.

This paper is divided into four parts. The first part is to compare and sort out the development history of domestic satellite remote sensing image denoising methods. The second part is to build remote sensing noise model and remote sensing image big data denoising model combining DTCWT and fourth-order partial differential equation. The third part is to design and carry out experiments to verify the denoising performance of the designed denoising method and other comparison methods for remote sensing images. The fourth part is to analyze the experimental results, and summarize the advantages and disadvantages of the denoising methods designed in this study and the improvement direction.

2. Related Works

University professors at home and abroad and front-line technical experts in the industry have carried out a lot of research to optimize the processing accuracy of satellite remote sensing images and the performance of image denoising algorithms. Lenin et al. proposed an automatic classification algorithm for handholding based on EMG signals based on advanced wavelet transform. In this algorithm, symlet wavelet is used to denoise the EMG signal on the subject's body, and then the dimension is reduced. In addition, lifting wavelet transform and DTCWT are used to extract the important attributes of the signal, and neural networks, support vector machine, and other algorithms are used to construct multiple classifiers. The calculation results of the test data set show that the improved algorithm can effectively optimize the recognition performance of the system for EMG signals [8]. Wang et al. believed that early detection and treatment of breast cancer can reduce the mortality of breast cancer, but the existing microcalcification feature extraction methods can only successfully extract features under certain specific conditions, and cannot accurately express all the information of the target region. Therefore, the research team proposed a data feature extraction algorithm based on DTCWT and texture information. After testing, it is found that the algorithm designed in this study can achieve better results in mammogram image denoising than the traditional algorithm, and its robustness is also superior [9]. He et al. designed a state recognition method of zinc rapid roughing process based on dual-tree complex wavelet transform, and the test found that this improved algorithm could improve the state recognition accuracy of zinc rapid roughing process [10]. Goyal and Meenpal proposed a kinship recognition algorithm for similar full-face images based on improved DTCWT. By analyzing the simulation data, it is found that the method designed in this study has certain application value in all kinship data sets. Specifically, the average kinship accuracy of this algorithm on two commonly used face data sets is 95.85% and 95.30%, respectively [11].

Raissi and Karniadakis proposed a partial differential equation-based algorithm that can learn from small data, in which a hidden physical model is introduced, which is essentially an efficient data learning machine capable of exploiting time-dependent and nonlinear partial differential. Equations represent the laws of physics and can extract patterns from experimentally generated high-dimensional data. The method can be applied to problems such as learning of partial differential equations, system identification, or data-driven. The framework of the algorithm relies on a Gaussian process, which enables the algorithm to strike a balance between model complexity and data fitting. By using the algorithm to solve a variety of canonical problems across multiple scientific fields, the proposed method is found to be effective, and the method can operate under complex computing conditions without requiring large amounts of data to support training [12]. Wu and Xu proposed a single-solvent property identification model based on simplex networks and partial differential equations, and used the data of the two-dimensional third harmonic problem to study the performance of the model, image recognition accuracy [13]. Mcdonald et al. discussed the time-dependent partial differential equation problem and proposed a block loop-preprocessing algorithm for the data processing system with block Toeplitz structure. The algorithm obtains symmetric data by reordering the variables, and can strictly establish the convergence boundary of the problem, thus ensuring that the number of iterations of all systems has no correlation with the time variables. The algorithm is verified by public data sets. It is found that the algorithm can significantly improve the data cleaning efficiency of the data processing system with block Toeplitz structure [14]. Feng et al. found that data filtering and other technologies are generally used in the industry to obtain high spatial quality images. The precision of remote sensing image obtained by super-resolution method cannot meet the application well. In order to solve this problem, a high spatial quality remote sensing image reconstruction algorithm based on fusion generation countermeasure network is designed. The algorithm improves the image quality by integrating the denoising and super-resolution methods into a computing model. Then, tests were carried out using a variety of data sets, and the results showed that the algorithm has certain application value in acquiring remote sensing images [15]. Ma et al. found that the current commonly used denoising methods have not reached sufficient robustness in practice because they ignore the inherent structure of remote sensing images or underestimate the difficulty of processing environmental noise to a certain extent. Therefore, a new denoising algorithm is proposed in this study, which uses the robust noise and inherent characteristics of the image to establish an image-processing model. The performance test of this algorithm shows that the algorithm designed in this study has certain advantages compared with the most advanced methods [16].

To sum up, in order to improve the image denoising efficiency and denoising performance, experts and scholars at home and abroad have used DTCWT method and partial differential equation to build a variety of denoising algorithms. However, it is difficult to smooth the noise in the depression area by using partial differential equation only. The advantage of this method is the overall denoising of the image. At the same time, the advantage of DTCWT method is that it can focus the high-frequency detail components in all directions of the image and has good time-frequency localization characteristics. Therefore, this study attempts to combine the two to build a new satellite remote sensing image data-denoising algorithm, hoping to improve the denoising ability of the algorithm.

3. Design of a Big Data Denoising Model for Remote Sensing Images Based on DTCWT and Fourth-Order Partial Differential Equations

3.1. Remote Sensing Image Noise Model and Discrete Wavelet Transform Design. In this study, the noise model affected by remote sensing was first designed, and the advantages and disadvantages of discrete wavelet transform were analyzed to prepare for the later proposed remote sensing image big data-denoising model combining DTCWT and partial differential equations. Since the working state of the sensor is affected by several environmental factors and system components, the remote sensing effect may be polluted by some noise in the process of transmission and acquisition. Assuming that the noise-free grayscale image is the noise $f(x, y)$ in $n(x, y)$ the graph, and the noise-containing image is $g(x, y)$, the multiplicative noise form of the noise-containing image can be expressed as $g(x, y) = f(x, y)[1 + n(x, y)]$ [17–19]. The noise in the image is composed of Gaussian noise and salt and pepper noise. The former is mainly caused by the electronic circuit noise caused by factors such as high temperature and low illumination in the environment, and the probability density function obeys a normal distribution [20]. The latter is caused by improper equipment operation, and the probability density function of noise is shown $p(q)$ in the following:

$$p(q) = \begin{cases} P_c, z = c, \\ P_d, z = d, \\ 0, \text{else}. \end{cases} \tag{1}$$

In Equation (1), $p(q)$ and b, respectively, represent the noise point, q represents the pixel gray value in the image, and $p(q)$ represents the probability of occurrence, and satisfy $0 \le P_c \le 1$, b, and $p(q)$, respectively, $0 \le P_d \le 1$. Therefore, $d > cd$ the pixel point with the gray value at that time can be regarded as a bright noise point, or "salt noise," and the pixel point $d \le c$ with the gray value at that time is considered c as a "pepper noise" or a dark noise point.

This research needs to apply wavelet transform to two-dimensional image processing. The input signal in this task is two-dimensional discrete signal. Therefore, the wavelet decomposition and reconstruction transformation method for discrete two-dimensional image data is designed in the following. If the function $\Phi(t_1, t_2) \in L^2(R^2)$ meets the conditions $\int\int_{-\infty}^{+\infty}\Phi(t_1, t_2)\mathrm{d}t_1 t_2 = 0$, $\Phi(t_1, t_2)$ is called the generating function of the two-dimensional wavelet, and the function can be expanded and translated to obtain a small fundamental wave group, such as

$$\Phi_{a,b_1,b_2}(t_1, t_2) = \frac{1}{a}\Phi\left(\frac{t_1 - b_1}{a}, \frac{t_2 - b_2}{a}\right), a > 0; b_1, b_2 \in R. \tag{2}$$

In Equation (2), a, b_1, and b_2 represent the scale factor and the translation factor in two different directions, respectively. At that time, $x(t_1, t_2) \in L^2(R^2)x(t_1, t_2)$ the two-dimensional wavelet transform of the signal can be expressed as follows:

$$\mathrm{WT}_x(a, b_1, b_2) = \frac{1}{a}\int_{-\infty}^{+\infty}\int_{-\infty}^{+\infty} x(t_1, t_2)\Phi\left(\frac{t_1 - b_1}{a}, \frac{t_2 - b_2}{a}\right)\mathrm{d}t_1\mathrm{d}t_2. \tag{3}$$

The discretization of the $a = a_0^j$ parameters a, t_1, and the three values are, respectively t_2, $b_1 = a_0^j k_1 \tau_0$, $b_2 = a_0^j k_2 \tau_1$, where τ_1 and τ_2 are the system parameters of the auxiliary transformation, and $f(t_1, t_2)$ the discrete wavelet change formula of the two-dimensional function can be obtained by combining Equation (3), see the following equation:

$$\mathrm{WT}_f(a_0, \tau_0, \tau_1) = a_0^{-j/2}\iint f(t_1, t_2)\Phi \cdot \left(a_0^{-j}t_1 - k_1\tau_0, a_0^{-j}t_2 - k_2\tau_1\right)\mathrm{d}t_1\mathrm{d}t_2. \tag{4}$$

Therefore, it can be seen that the essence of the two-dimensional wavelet transform is to attach importance to the one-dimensional signal in each row and column of the image, and use low-pass and high-pass filtering on them, respectively. To sum up, the calculation flow of the two-dimensional discrete wavelet decomposition is shown in Figure 1.

As shown in Figure 1, the two-dimensional discrete wavelet decomposition algorithm first decomposes the image x into two subbands $h_0(x)$, $h_1(x)$, according to the dimension, and then each component y is divided into two subbands $h_0(y)$ and $h_1(y)$. According to the dimension, "$*$" represents the interval sampling step, then the image will eventually be decomposed into 4 subbands LL, LH, HL, and HH. The subband reconstruction method after 2D discrete wavelet decomposition is shown in Figure 2.

"#" in Figure 2 represents the reverse operation of sampling at intervals. As shown in Figure 2, the subband reconstruction process after 2D discrete wavelet decomposition is generally consistent with the decomposition process. In this process, the horizontal high-frequency subband, the vertical high-frequency subband, the low-frequency subband, and the diagonal high-frequency subband will finally be synthesized into the original image after denoising.

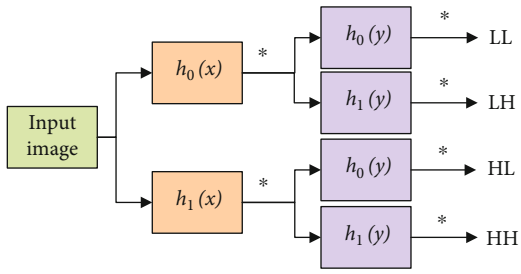

Figure 1: Flow chart of 2D discrete wavelet decomposition calculation.

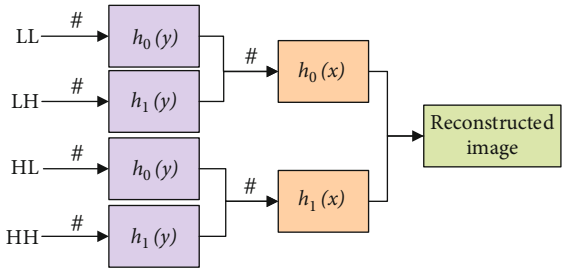

Figure 2: Reconstruction flow chart of 2D discrete wavelet decomposition subband.

3.2. Denoising Model Design Combining DTCWT and Partial Differential Equation. Due to the various application limitations of discrete wavelet change, for example, this method is highly sensitive to translation operations, and can transform in less directions, so it cannot achieve complete data reconstruction [21]. Therefore, in order to overcome the above shortcomings, some scholars proposed the DTCWT method, which not only has good time-frequency analysis ability of data signals but also has translation invariance, supports complete reconstruction, and has more decomposition directions [22, 23]. The DTCWT method adopts the structure of binary tree to decompose the image, and uses two filters to generate sampling delay in the first layer of decomposition, so that it can offset the lost sampling information in the second layer [24]. The one-dimensional and two-dimensional DTCWT reconstruction process in the DTCWT method are, respectively, designed as follows, for the subsequent construction of the denoising algorithm. The wavelet odd function in the DTCWT method is defined in complex form, as shown in the following:

$$\Phi(t) = \Phi_r(t) + j\Phi_i(t). \tag{5}$$

In Equation (5), $\Phi_r(t)$ and $\Phi_i(t)$ represent the real function, which, respectively, constitutes the real part and imaginary part of the complex wavelet. For any arbitrary $f(t) \in L^2(R)$, DTCWT can be expressed as $\langle f, \Phi_c \rangle = \langle f, \Phi_h \rangle + \langle f, \Phi_g \rangle$, correspondingly exists $d_c(j,n) = d_h(j,n) + \mathrm{jd}_g(g, n)$, where j represents the resolution, $d_h(j,n)$ and $d_g(g,n)$ are the real and imaginary parts of the complex wavelet transform coefficients, respectively, and $d_c(j,n)$ as the magnitude and phase of Equation (7) expression.

$$|d_c(j,n)| = \left([d_n(j,n)]^2 + [d_g(j,n)]^2 \right)^{1/2}, \tag{6}$$

$$\angle d_c(j,n) = \arctan\left(\frac{d_h(j,n)}{d_g(j,n)} \right). \tag{7}$$

The one-dimensional DTCWT method is shown in Figure 3. In Figure 3, $g_0(n)$ and $g_1(n)$, respectively, represent the conjugate integral filter pair, $h_0(n)$ and $h_1(n)$, respectively, represent the conjugate quadrature filter pair. As shown in Figure 3, the data is first transformed into a complex wavelet form, and then the real part and the imaginary part of the complex wavelet are separated. Then two sets of filters are used to generate the real and imaginary transform coefficients, respectively. In addition, after each layer is decomposed, six high-frequency information components and one low-frequency information component in different directions can be obtained [25].

Figure 4 shows the reconstruction process of the DTCWT method. The reconstruction process is also carried out in the form of two trees. One tree is used to construct the real and imaginary number structures of the object. The final output of the reconstruction step is the average value of the real and imaginary part signals.

The two-dimensional DTCWT is generally similar to the one-dimensional DTCWT as described. The one-dimensional data can be converted into a two-dimensional data by using the wavelet tensor product. The conversion process is designed in the following. For $\Phi(t) = \Phi_r(t) + j\Phi_i(t)$, the data two-dimensional dual-tree complex wavelet can be expressed as follows:

$$\begin{aligned} \Phi(x,y) = {} & \Phi_h(x)\Phi_h(y) - \Phi_g(y)^2 \\ & + j\left[\Phi_g(x)\Phi_h(y) + \Phi_h(x)\Phi_g(y)\right]. \end{aligned} \tag{8}$$

Observing Equation (8), it can be seen that the real part of the two-dimensional data is composed of the difference between two two-dimensional separable wavelets. In the same way, all the two-dimensional data expressions of the information can be obtained, and the real parts of these complex wavelets can be $1/\sqrt{2}$ planned and processed to obtain six two-dimensional real wavelets. Dimensional real wavelet, so far, the calculation method of two-dimensional data coefficients with six directions is completed.

In the following, another method for constructing the final denoising model, namely the fourth-order partial differential denoising model, will be described. Since the second-order partial differential denoising model will be calculated towards the segmented plane, there will be a "staircase" effect. The fourth-order partial differential denoising model approximates the original image by a segmented slope, which can better solve the mentioned problems. The energy functional calculation method of this model is shown in the following:

$$E(u) = \int_{\Omega} f\left(\left|\nabla^2 u\right|\right) d\Omega. \tag{9}$$

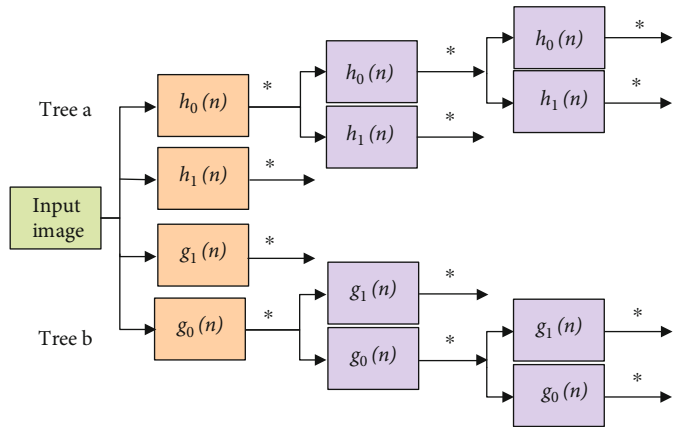

Figure 3: Schematic diagram of the decomposition process of the one-dimensional DTCWT method.

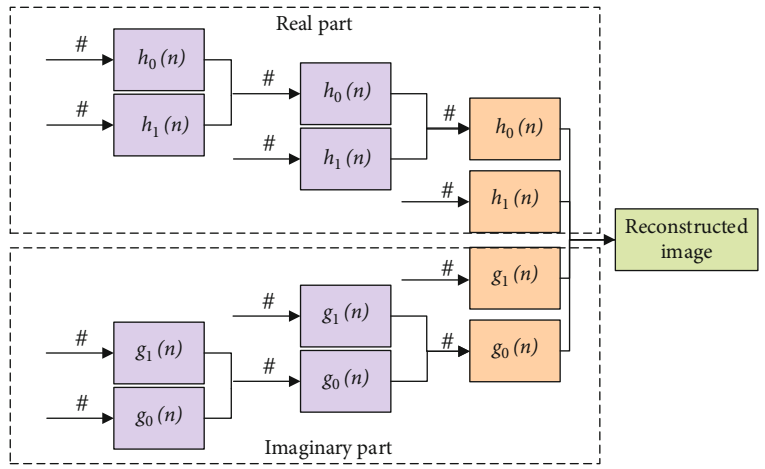

Figure 4: Schematic diagram of the reconstruction process of the one-dimensional DTCWT method.

Equation (9) ∇^2 represents the Laplacian operator, which ∇^2 represents the smoothness of the image, which $f'(.) > 0$ is ∇^2 a monotonically increasing function, so there is a minimum ∇^2, which can make $E(u)$ the minimum value, and the $E(u)$ minimum is the process of image smoothing, $E(u)$ the Euler-Lagrange equation. The form is shown in the following:

$$\frac{\partial^2}{\partial x^2}\left(f'\left(\left|\nabla^2 u\right)\right|u_{xx}\right) + \frac{\partial^2}{\partial y^2}\left(f'\left(\left|\nabla^2 u\right)\right|u_{yy}\right) = 0. \quad (10)$$

Combining Equations (9) and (10), Equation (11) can be further derived as

$$\nabla^2\left[f'\left(\left|\nabla^2 u\right|\right)\frac{\nabla^2 u}{\left|\nabla^2 u\right|}\right] = 0. \quad (11)$$

Because of the diffusion function, $g(x) = f'(x)/x$.

$$\nabla^2\left[g\left(\left|\nabla^2 u\right|\right)\nabla^2 u\right] = 0. \quad (12)$$

Using the gradient descent method to solve Equation (12) and introducing the time t variable, the gradient descent flow can be expressed using the following equation:

$$\frac{\partial u(x, y, t)}{\partial t} = \operatorname{div}\left(g\left(\left|\nabla^2 u\right|\right)\nabla^2 u\right). \quad (13)$$

So far, the improved denoising model has been designed, which can effectively reduce the step effect caused by the filtering process of the second-order partial differential equation, and retain the texture information of the image.

3.3. Improve the Design of the Big Data Denoising Model for Remote Sensing Images. Since the edges of objects and most of the noise in the remote sensing image big data are distributed in the high-frequency subbands, it is difficult to smooth the noise in the concave area simply by using partial differential equations. At the same time, the advantage of DTCWT method is that it can focus the high-frequency detail components in all directions of the image, and has good time-frequency localization characteristics. Therefore,

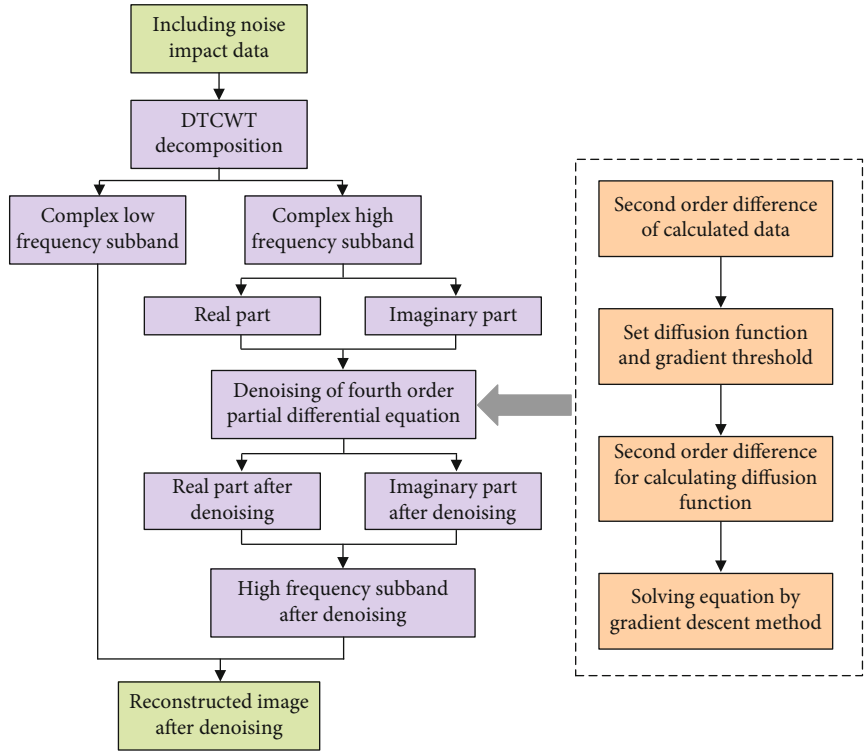

Figure 5: Flow chart of FD-DTCWT remote sensing image big data denoising model.

this study proposes a large data-denoising model for remote sensing images that combines the DTCWT method with the fourth-order partial differential equation dual tree complex wavelet transform (FD-DTCWT). The core part of the FD-DTCWT denoising model includes multiscale image data decomposition and partial differential equation data filtering based on the FD-DTCWT method, which are designed in detail.

In the FD-DTCWT denoising model, the Q-shift filter bank is used to perform one-dimensional DTCWT decomposition on the noisy remote sensing image, and six and one high-frequency and low-frequency data sets are obtained, respectively. The former contains a large amount of image noise and edge information. The specific one-dimensional DTCWT decomposition process of remote sensing image big data has been shown in the previous content, and will not be described here.

The solution of partial differential equations is generally carried out by the finite difference method. The main calculation steps of the finite difference method are to discretize the time area and the space area, and use the difference calculated according to the pixel gray value to approximately replace the derivative of each grid point. According to the derived iterative formula, select the appropriate number of iterations to solve the approximate solution of the partial differential equation. Specifically, the iterative solution equation described by Equation (13) is first discretized, and the second-order difference $\nabla^2 u|_{i,j} =$ calculation of the image gray value at the center point is shown in the following:

$$\nabla^2 u\big|_{i,j} = (k_{xx})_{i,j} + (k_{yy})_{i,j}. \tag{14}$$

The $(k_{xx})_{i,j}$ calculation method is shown in the following:

$$(u_{xx})_{i,j} = \frac{k_{i+1,j} + k_{i-1,j} - 2k_{i,j}}{m^2}. \tag{15}$$

In Equation (15), m represents the space step size of discretization, select a diffusion function $g(|\nabla u|)$, and its second-order difference form is shown in the following:

$$\nabla^2 g_{i,j}^{k+1} = \frac{\left(j_{i+1,j}^k + j_{i-1,j}^k + j_{i,j-1}^k + j_{i,j+1}^k + 4j_{i,j}^k\right)}{m^2}. \tag{16}$$

Therefore, the iterative formula after discretizing Equation (13) is shown in the following:

$$u^{k+1} = u^k - \Delta t\left(\nabla^2 g\left(\left|\nabla^2 u^k\right|\right)\nabla^2 u^k\right). \tag{17}$$

In Equation (17), Δt represents the time step of discretization. Combining the mentioned contents, a remote sensing image big data-denoising model can be designed and obtained by combining the DTCWT method and partial differential. The algorithm flow is shown in Figure 5.

As shown in Figure 5, after the model inputs image big data, it is necessary to first determine the iteration discrete time step, space step, and iteration number. Step 2 uses Q-shift filter to decompose DTCWT into real part and imaginary part. Step 3 uses the decomposed high-frequency subband to perform gray level second-order difference calculation or denoise the decomposed subband to obtain $\nabla^2 u|_{i,j}$. Step 4 selects the diffusion function and gradient

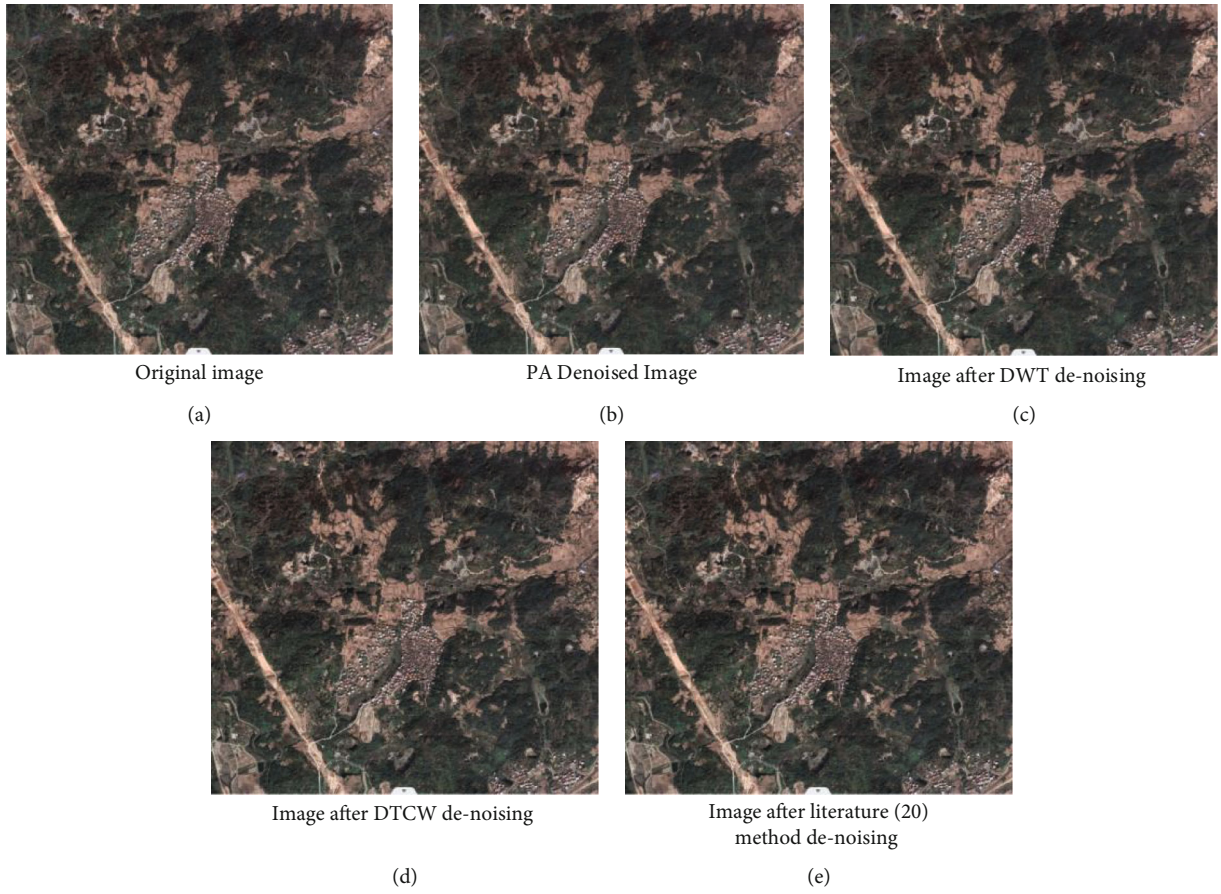

Figure 6: Example of satellite remote sensing image processing.

threshold K. Then, use Equation (16) to calculate the second-order difference of the diffusion function, and then use Equation (17) to iterate to the set number of times to obtain the denoised high-frequency wavelet coefficient YH'. Finally, use the denoised complex high-frequency subband, complex low-frequency subband components, and complex low-frequency subband to perform dual tree complex wavelet reconstruction, and output the denoised remote sensing big data image.

4. Comparative Experimental Analysis of Model Denoising Performance

Now, start the experiment to test the noise removal ability of the model. In this study, research team members selected a number of satellite remote sensing image data with clear images, good quality, and some real noise obtained from relevant national public utilities as the experimental data set. The image in the data set is taken by the civil meteorological satellite, the shooting equipment is an optical camera, and the pixel specification of the image is 1024×1024 pixels. The data set is divided into test set and training set according to 3 : 7, and the division method is random selection. The selected satellite images contain information about roads, buildings, farmland, roads, factories, and other objects, which are representative. Combined with the hardware specification, a remote sensing image big data-denoising model is built on the software-programming platform of Python 3.0 programming language, and the model is run in an environment with a CPU of i7-8700, a memory size of 8 GB, and an operating system of Windows 10. In the experiment, Python language package is used to add different noise variances to the image, and the pure anisotropy (PA) model commonly used in the industry. The denoising model of discrete wavelet transform combined with fourth-order partial differential equation (FD-DWT) is used as the contrast model, and parallel experiments are conducted with the FD-DTCW model designed in this study. In the experiment, the signal-to-noise ratio, calculation time, peak signal-to-noise ratio, structural similarity, and root mean square error were selected as evaluation indicators. In order to reduce the difficulty of statistics, some indicators need to be normalized. In addition to root mean square error, their values and indicators are displayed by taking the average value of each test set sample. When the noise variance is 0.03, the original image and a case satellite remote sensing image processed by each method are shown in Figure 6.

It can be seen from Figure 6 that there is a lot of noise in the original image, and the image noise after denoising by PA, literature [26] method, FD-DWT, and FD-DTCW methods has been improved to varying degrees. Among which, the image noise points after processing by FD-DTCW method have been significantly reduced, and the

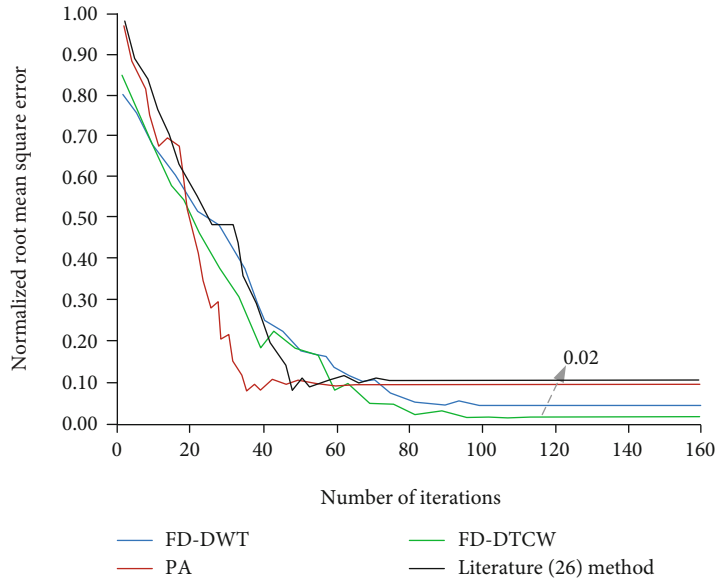

Figure 7: Variation of the root mean square error of each model during the training process.

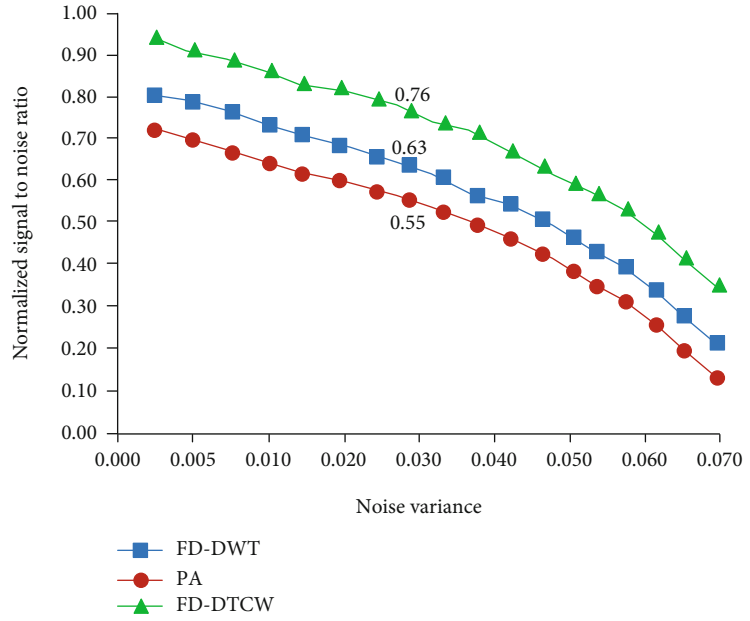

Figure 8: Changes in the signal-to-noise ratio of each model on the test set.

denoising effect is the most significant. Next, analyze the change of root mean square error of each model on the training data set, as shown in Figure 7.

In Figure 7, the horizontal axis is used to describe the number of iterations, and the vertical axis is used to describe the root mean square error value after normalization. Different colors represent different remote sensing big data denoising models. It can be seen from Figure 6 that with the increase of model training rounds, the normalized root mean square error values of each model on the test set show a change rule that decreases significantly at first, and then tends to be stable. When the number of iterations exceeds 100, the root mean square errors of the three models converge. At this time, the normalized root mean square errors of FD-DWT model, PA model, FD-DTCW model, and literature [26] model are 0.05, 0.09, 0.02, and 0.10, respectively. The normalized root mean square error of the FD-DTCW model designed in this study is the smallest, which shows that the image data after denoising and reconstruction has the least information loss, and the original image information retained is the most. Next, we will start to analyze the performance of each denoising model after training on the remote sensing image big data test set. See Figure 8 for the statistical results of the signal-to-noise ratio. Note that the performance of the advanced method in Figure 7, the literature [26] model, is the worst. To simplify the experimental process, this method will not be considered in the subsequent analysis.

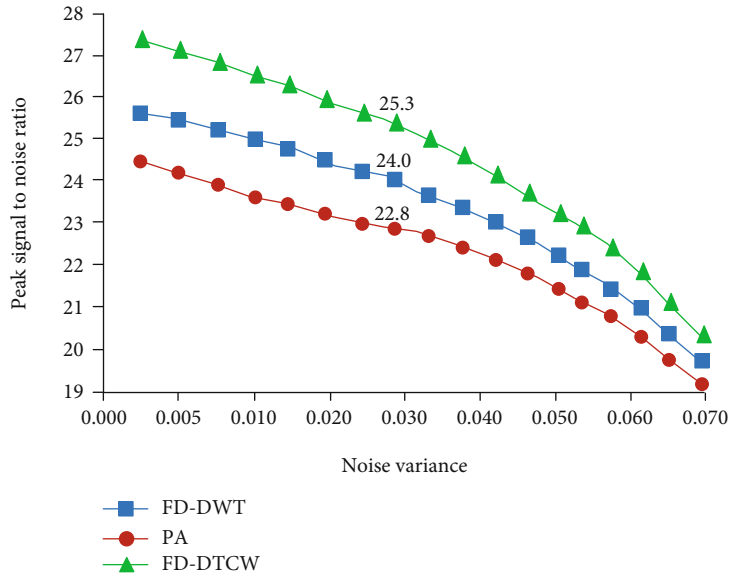

Figure 9: The variation of peak signal-to-noise ratio of each model on the test set.

The horizontal axis in Figure 8 describes the noise variance set in Python environment, and the vertical axis represents the normalized signal-to-noise ratio of the calculated results of the trained model on the test set. Note that the horizontal axis is set in the form of uneven distribution in order to show the change law of the graph as clearly as possible. It can be seen from Figure 8 that with the increase of noise variance, the output normalized signal-to-noise ratio of each model on the test set shows an accelerated downward trend, that is, the denoising effect is gradually worse. This is because the larger the noise variance, the more serious the noise interference of the representative image, and the denoising effect of the model will be correspondingly weakened. However, when the noise variance is fixed, the FD-DTCW model designed in this study has the best denoising effect, followed by the FD-DWT model. For example, when the noise variance is 0.030, the normalized signal-to-noise ratios of FD-DWT model, PA model, and FD-DTCW model are 0.63, 0.55, and 0.76, respectively. This is because in each subband decomposed by the DTCWT method, the method designed in this study only denoises the complex high-frequency subband containing a lot of noise, which avoids unnecessary information loss to a greater extent. Next, the performance of each model is analyzed from the perspective of peak signal-to-noise ratio. See Figure 9 for the statistical results.

The horizontal axis in Figure 9 describes the noise variance set in Python environment, and the vertical axis is used to describe the normalized signal-to-noise ratio of the calculated results of the trained model on the test set. Note that the horizontal axis is set in the form of uneven distribution in order to show the change law of the graph as clearly as possible. It can be seen from Figure 9 that when the noise variance parameter increases continuously, the output normalized signal-to-noise ratio of each model on the test set shows an accelerated downward trend, that is, the denoising effect becomes worse. This is because the larger the noise variance, the more serious the noise interference of the representative image, and the denoising effect of the model will be weakened accordingly. However, when the noise variance is fixed, the FD-DTCW model designed in this study has the best denoising effect, followed by the FD-DWT model. For example, when the noise variance is 0.030, the normalized signal-to-noise ratios of FD-DWT model, PA model, and FD-DTCW model are 0.63, 0.55, and 0.76, respectively. Next, the performance of each model is analyzed from the perspective of peak signal-to-noise ratio. See Figure 10 for the statistical results.

The vertical axis in Figure 10 represents the structural similarity of the test set images. Looking at Figure 10, the slope of the structural similarity curve output by each denoising model is always less than 0, and it first decreases and then increases, and tends to stable, the inflection point of the curve is roughly in the range of noise variance 0.020~0.040 with the increase of noise variance. It shows that with the increase of noise severity, the reconstructed image after denoising of each model is less similar to the source image and loses more information. However, when the noise method is the same, the FD-DTCW model retains the most original image information. For example, when the noise variance is around 0.030, the structural similarity of the FD-DWT model, the PA model, and the FD-DTCW model is 0.64, 0.57, and 0.74, respectively. Then, compare the figure of Merit (FOM) of each denoising model, as shown in Figure 11.

It can be seen from Figure 11 that with the increase of noise variance, the FOM value change of the test set image processed by each denoising method is generally consistent with Figure 10. Because of the increase of noise severity, the edge information quality of the image will inevitably decline as a whole, leading to the decline of the corresponding index FOM value. When the noise variance is 0.030, the FOM of FD-DWT model, PA model, and FD-DTCW model are 0.79, 0.76, and 0.84, respectively. Finally, compare the

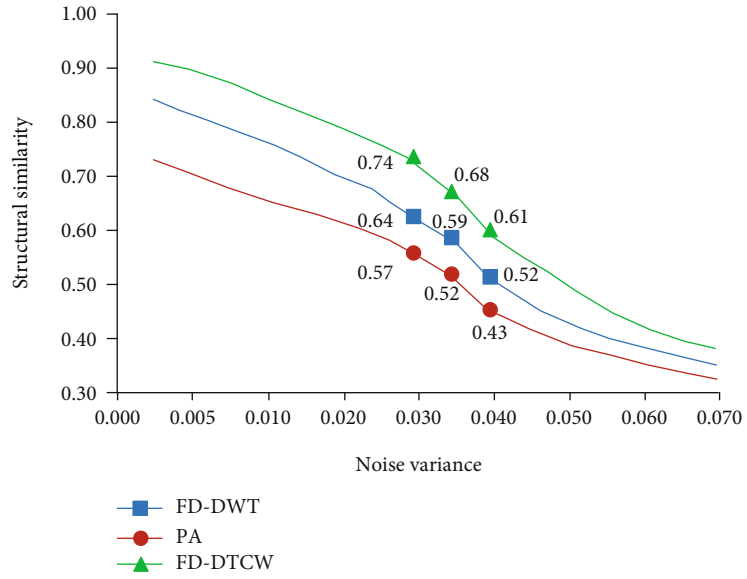

Figure 10: Changes in the structural similarity of each model on the test set.

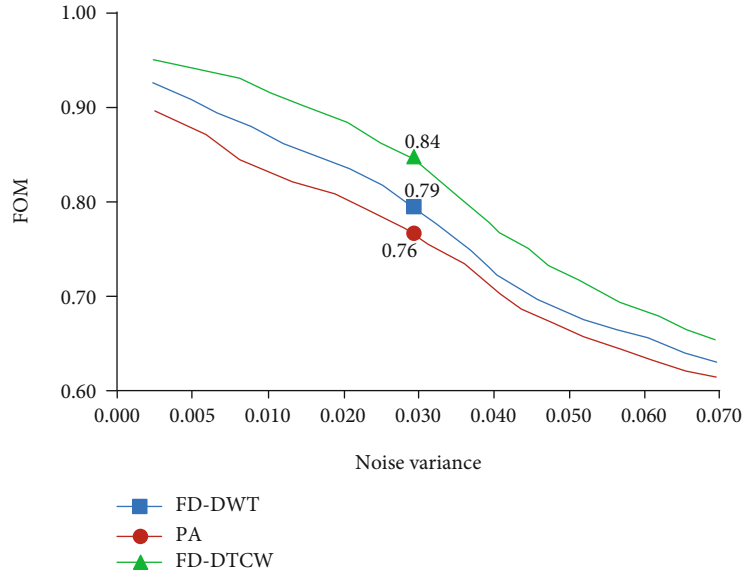

Figure 11: FOM changes of each model on the test set.

data processing efficiency of each denoising model, and calculate the model calculation time consumption under different processing samples, as shown in Figure 11. Finally, compare the data processing efficiency of each denoising model, and calculate the model calculation time consumption under different processing samples, as shown in Figure 12.

Note that in order to ensure the accuracy of the experimental results, each experimental method is repeated for 10 times, and the results are displayed using the mean and standard deviation of the calculation time. F difference significance test was conducted for the time consuming data of group sample size calculation, and the significance was set as 0.05. It can be seen from Figure 12 that under various sample sizes, the calculation time of PA model is the least, followed by FD-DWT model, and the calculation time of FD-DTCW model is the longest, with a significant difference from that of the previous two algorithms. It shows that the method proposed in this study is slightly higher in computational complexity than its method. But on the whole, the calculation time of the latter is still small, which can meet the application requirements. In addition, the larger the noise variance is, the longer the calculation time of each method is. In the common noise variance range of 0.01~0.05, there is an order of magnitude difference between the time of processing the same number of samples with the same method and the time of processing 0.03 noise variance. In order to further verify the effectiveness of the methods proposed in this study, FAIR1M, a large satellite remote sensing image data set published by the Chinese government, containing more

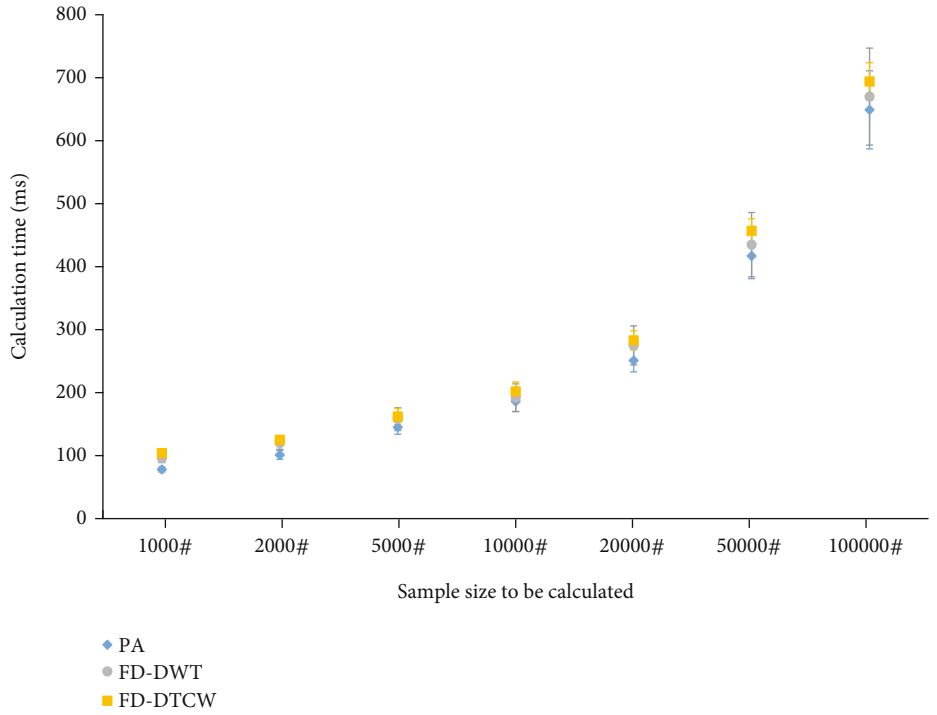

Figure 12: Time consumption of model calculation under different number of samples to be processed (unit: ms).

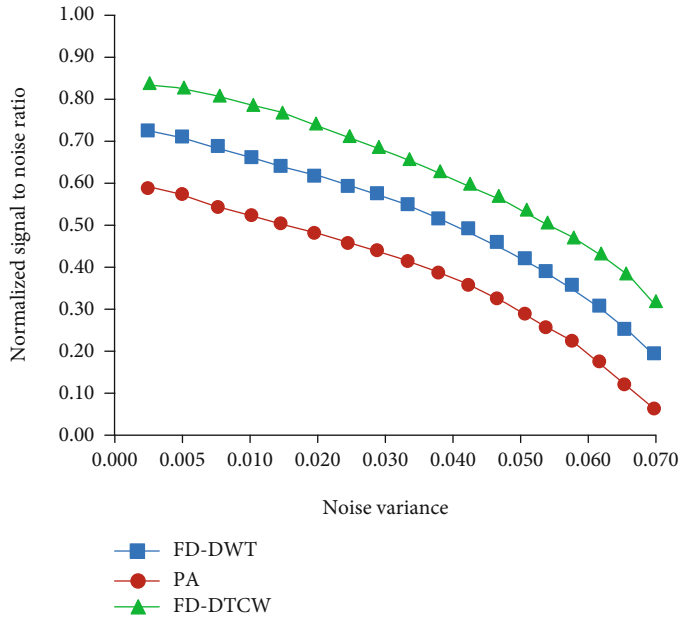

Figure 13: Signal to noise ratio change of each model on FAIR1M test set.

than one million target details, was selected, and the project was deployed and run on the big data analysis software platform Spark. Figure 13 was obtained through analysis.

The horizontal axis, vertical axis, and data line styles in Figure 13 are consistent with those in Figure 8. It can be seen from Figure 12 that with the increase of noise variance, the output normalized signal-to-noise ratio of each model on the test set still shows a downward trend. However, the signal-to-noise ratio of the image processed by FD-DTCW method is obviously higher than that of other methods. Moreover, when the noise variance is the same, FD-DTCW model has the best denoising effect, followed by FD-DWT model. For example, when the noise variance is 0.030, the normalized signal-to-noise ratios of FD-DWT model, PA model, and FD-DTCW model are 0.62, 0.47, and 0.75, respectively.

5. Conclusion

Due to the unstable working state of the sensor and improper equipment operation, there is often some noise in satellite remote sensing images, which will affect the use of subsequent images. Therefore, this research combined the fourth-order partial differential equation and the DTCWT method to design an improved satellite remote sensing big data image-denoising model. The experimental results of denoising based on real satellite remote sensing data show that the normalized signal-to-noise ratios of FD-DWT model, PA model, and the denoising model FD-DTCW designed in this study are 0.63, 0.55, and 0.76, the peak signal-to-noise ratios were 24.0, 22.8, and 25.3, and the structural similarity was 0.64, 0.57, and 0.74, respectively. At the same time, when the number of calculated samples is 100,000, the calculation time of FD-DWT model, PA model, and FD-DTCW model is 670 ± 77, 649 ± 62, and 694 ± 30, respectively. Although the design model of this research takes the most time, the difference from the comparison model is smaller. The experimental data proves that the denoising model of satellite remote sensing big data image designed in this study has better denoising performance than the common denoising model, but the calculation speed is slightly slow, which is also the main limitation of the method designed in this study. The future work direction is to reduce the overall complexity of the algorithm to shorten the image denoising time on the premise of continuously improving the denoising performance of the method.

Data Availability

The data used to support the findings of this study are available within this article.

Conflicts of Interest

The author declares that there is no conflict of interest regarding the publication of this article.

References

[1] L. Teng, F. Xue, and Q. Bai, "Remote sensing image enhancement via edge-preserving multiscale retinex," *IEEE Photonics Journal*, vol. 11, no. 2, pp. 1–10, 2019.

[2] B. Du, Z. Huang, N. Wang, Y. Zhang, and X. Jia, "Joint weighted nuclear norm and total variation regularization for hyperspectral image denoising," *International Journal of Remote Sensing*, vol. 39, no. 2, pp. 334–355, 2018.

[3] L. Fu, C. Ren, X. He, X. Wu, and Z. Wang, "Single remote sensing image super-resolution with an adaptive joint constraint model," *Sensors*, vol. 20, no. 5, pp. 1276–1295, 2020.

[4] D. A. Grant, "Beam vibrations with time-dependent boundary conditions," *Journal of Sound & Vibration*, vol. 89, no. 4, pp. 519–522, 1983.

[5] W. Sweldens, "Lifting scheme: a new philosophy in biorthogonal wavelet constructions. Wavelet applications in signal and image prodcessing III," *International Society for Optics and Photonics*, vol. 2569, pp. 68–79, 1995.

[6] E. Le Pennec and S. Mallat, "Bandelet representations for image compression," in *Proceedings 2001 International Conference on Image Processing (Cat. No. 01CH37205)*, pp. 12–34, Thessaloniki, Greece, 2001.

[7] V. Velisavljevie, B. Beferull-Lozano, and M. Vetterli, "Space-frequency quantization for image compression with directionlets," *IEEE Transactions on Image Processing A Publication of the IEEE Signal Processing Society*, vol. 16, no. 7, pp. 1761–1773, 2007.

[8] A. H. Lenin, S. M. Vasanthi, and T. Jayasree, "Automated recognition of hand grasps using electromyography signal based on LWT and DTCWT of wavelet energy," *International Journal of Computational Intelligence Systems*, vol. 13, no. 1, pp. 1027–1035, 2020.

[9] Y. Wang, B. Wu, N. Zhang, J. Liu, F. Ren, and L. Zhao, "Research progress of computer aided diagnosis system for pulmonary nodules in CT images," *Journal of X-Ray Science and Technology*, vol. 28, no. 1, pp. 1–16, 2020.

[10] Z. He, Z. Tang, Z. Yan, and J. Liu, "DTCWT-based zinc fast roughing working condition identification," *Chinese Journal of Chemical Engineering*, vol. 26, no. 8, pp. 1721–1726, 2018.

[11] A. Goyal and T. Meenpal, "Patch-based dual-tree complex wavelet transform for kinship recognition," *IEEE Transactions on Image Processing*, vol. 30, no. 1, pp. 191–206, 2021.

[12] M. Raissi and G. E. Karniadakis, "Hidden physics models: machine learning of nonlinear partial differential equations," *Journal of Computational Physics*, vol. 357, no. 3, pp. 125–141, 2018.

[13] S. Wu and J. Xu, "Nonconforming finite element spaces for $2m$th order partial differential equations on $\mathbb{R}^n$ simplicial grids when $\mathbb{m}=\mathbb{n}+1$," *Mathematics of Computation*, vol. 88, no. 316, pp. 531–551, 2019.

[14] E. Mcdonald, J. Pestana, and A. Wathen, "Preconditioning and iterative solution of all-at-once systems for evolutionary partial differential equations," *SIAM Journal on Scientific Computing*, vol. 40, no. 2, pp. A1012–A1033, 2018.

[15] X. Feng, W. Zhang, X. Su, and Z. Xu, "Optical remote sensing image denoising and super-resolution reconstructing using optimized generative network in wavelet transform domain," *Remote Sensing*, vol. 13, no. 9, pp. 1858–1880, 2021.

[16] T. H. Ma, Z. Xu, and D. Meng, "Remote sensing image denoising via low-rank tensor approximation and robust noise modeling," *Remote Sensing*, vol. 12, no. 8, pp. 1278–1281, 2020.

[17] A. Khmag, "Additive Gaussian noise removal based on generative adversarial network model and semi-soft thresholding approach," *Multimedia Tools and Applications*, vol. 81, pp. 1–21, 2022.

[18] A. Khmag, S. A. R. Al Haddad, R. A. Ramlee, N. Kamarudin, and F. L. Malallah, "Natural image noise removal using nonlocal means and hidden Markov models in transform domain," *The Visual Computer*, vol. 34, no. 12, pp. 1661–1675, 2018.

[19] J. Pushparaj and M. Malarvel, "Panchromatic image denoising by a log-normal-distribution-based anisotropic diffusion model," *Journal of Applied Remote Sensing*, vol. 13, no. 1, pp. 1–4, 2019.

[20] S. Yu, "Sonar image target detection based on deep learning," *Mathematical Problems in Engineering*, vol. 2022, Article ID 5294151, 11 pages, 2022.

[21] H. Wang, J. Wang, F. Yao, Y. Ma, L. Li, and Q. Yang, "Multiband contourlet transform for adaptive remote sensing image

denoising," *The Computer Journal*, vol. 63, no. 7, pp. 1084–1098, 2020.

[22] F. Yang, X. Chen, and L. Chai, "Hyperspectral image destriping and denoising using stripe and spectral low-rank matrix recovery and global spatial-spectral total variation," *Remote Sensing*, vol. 13, no. 4, pp. 827–845, 2021.

[23] S. Li, J. Zhao, H. Zhang, Z. Bi, and S. Qu, "A non-local low-rank algorithm for sub-bottom profile sonar image denoising," *Remote Sensing*, vol. 12, no. 14, p. 2336, 2020.

[24] P. Liu, M. Wang, L. Wang, and W. Han, "Remote-sensing image denoising with multi-sourced information," *IEEE Journal of Selected Topics in Applied Earth Observations and Remote Sensing*, vol. 12, no. 2, pp. 660–674, 2019.

[25] H. Shen, X. Li, L. Zhang, D. Tao, and C. Zeng, "Compressed sensing-based inpainting of aqua moderate resolution imaging spectroradiometer band 6 using adaptive spectrum-weighted sparse Bayesian dictionary learning," *IEEE Transactions on Geoscience & Remote Sensing*, vol. 52, no. 2, pp. 894–906, 2014.

[26] R. Ma, S. Li, B. Zhang, and H. Hu, "Meta PID attention network for flexible and efficient real-world noisy image denoising," *IEEE Transactions on Image Processing*, vol. 31, pp. 2053–2066, 2022.